Pergamon

Int. J. Heat Mass Transfer. Vol. 41, No. 3, pp. 513–527, 1998

Printed in Great Britain
0017–9310/98 $19.00+0.00

PII: S0017–9310(97)00196–8

Transitional reactor dynamics affecting optimization of a heat-driven metal hydride refrigerator

G. LLOYD and A. RAZANI

Mechanical Engineering Department, University of New Mexico, Albuquerque, NM 87131, U.S.A.

and

K. T. FELDMAN, JR

Thermal Electric Devices Inc., 1704 Stanford N.E., Albuquerque, NM 87106, U.S.A.

(*Received* 14 *March* 1997 *and in final form* 14 *June* 1997)

Abstract—This paper summarizes our research on modeling of metal hydride systems, examines the fundamental limitations imposed by geometrical and thermodynamic considerations, and presents a theoretical model for a complete system throughout an entire cycle. Apart from the assumption of local thermodynamic equilibrium no major simplifying assumptions are made and the non-ideal behavior of the hydrides is included. The nature of the heat and mass transfer processes as two coupled reactors are optimized is elucidated. The consequences for future metal hydride heat pump design are investigated.

1. INTRODUCTION

Metal hydrides (MHs) are ideal for solid–sorption heat pumps for several reasons: there are many MHs [1, 2]; environmental concerns continue to drive research on alternative technologies [3–5]; and a number of thermal cycles using the rapid kinetics of MHs [6] and the large compression ratios possible [7] have been studied. Finally, many complex material science and fabrication problems are being rigorously addressed [8–10]. The basis for MHs in thermal cycles is the van't Hoff equation [11]:

$$\ln p_{eq_{H_2}}(\text{atm}) = \frac{\Delta H(\text{J/kmole}_{H_2})}{\bar{R}T(\text{K})} - \frac{\Delta S(\text{J/kmole}_{H_2}\cdot\text{K})}{\bar{R}} \quad (1)$$

which represents the thermodynamic behavior for a two solid-phase, single gaseous phase system. Heat pump devices using MHs are conceptually simple and because of the large volume specific ΔHs and reversible absorption/desorption characteristics have been investigated experimentally and theoretically for over two decades. Despite this, a comprehensive understanding of these heat pumps remains elusive. This is due, in part, to the highly transient nature of the heat and mass transfer processes which occur in non-isothermal compressible flows in coupled porous reactors. Experimental study of solid–sorption systems, in general, is expensive, so there is a considerable need for a deeper analysis. Analytical investigations have focussed on specific aspects of a thermodynamic cycle and dwelled on simplifying assumptions [12], typically focusing on a single reactor. Accompanying these efforts has been a sequence of numerical models [13–24].

A general review [25] indicates a lack of effort towards understanding the process features of a complete system (two coupled reactors) undergoing a complete thermal cycle. There has been a tendency to invoke severe idealizations in geometry, to disregard spatial terms in the governing equations and to over-idealize boundary conditions. In addition, there has been little effort devoted towards understanding the role which the highly transient and inhomogeneous behavior, we term reactor dynamics, plays in reactor and system optimization. This paper will address some of these issues by examining global constraints (Section 2), formulating a system model (Section 3) that avoids many of the limitations imposed by earlier work and studying a numerical solution (Section 4). By doing so the relation between the transitional processes and how they influence the engineering potential of and problems which are likely to be encountered, as these systems mature further, can be appropriately studied, as discussed in Sections 5 and 6.

2. SYSTEM

The basic system is depicted in Fig. 1(a) with a cycle consisting of five sub-phases. One hydride, Fig. 1(c), is chosen with ΔH for H_2 compression by a reservoir of waste heat at T_{hot} during the phases $t_{1\to2}$ and $t_{2\to3}$; this reactor is usually called the *regenerator*. The other reactor employs a hydride, Fig. 1(b), such that at the ambient state it is thermochemically favorable for

NOMENCLATURE

A	reaction prefactor
A_0	core area [m^2]
COP	coefficient of performance
c	heat capacity [W·s/kg·K]
E_a	activation energy [J/kmole$_{H_2}$]
f	mass fraction [$kg_b/kg_{(c)}$]
F_Q	thermal waste fraction
$g(r, t)$	heat generation term [J/s·$m^3_{(c)}$]
ΔH	$\alpha \leftrightarrow \beta$ phase transition enthalpy [J/kmole$_{H_2}$]
h_c	reactant-to-reactor conductance [W/m^2·C]
h_{sf}	interstitial heat transfer coefficient [W/m^2·K]
h_∞	exterior convection coefficient
K	permeability [m^2]
k_{eff}	stagnant thermal conductivity [W/m·K]
L	reactor wall thickness [m]
L_p	characteristic particle size [m]
Lr	dimensionless mass source term
N_0	particle mass [kmole$_{hyd}$/particle$_{hyd}$]
P	average cooling power [W/kg$_{hyd}$]
$p(r, t)$	pore fluid pressure field [N/m^2]
Q	thermal energy [J]
r	radial space coordinate [m]
R_r	thermal containment resistance
$\bar{R}$	perfect gas constant, 8314 [J/kmole·K]
Re_p	particle Reynold's number
ΔS	phase transition entropy [J/kmole$_{H_2}$·K]
t	time coordinate [s]
$t_{1\to2}$	preheat phase of cycle
$t_{2\to3}$	charging phase
$t_{3\to4}$	equilibriation phase
$t_{4\to5}$	cooling phase
$t_{5\to6}$	equilibriation phase
Δt	timestep; process time [s]
$T(r, t)$	temperature [K]
T_∞	ambient reservoir temperature [K]
T_{cold}	temperature of cold reservoir [K]
T_{hot}	temperature of hot reservoir [K]
ΔU	internal energy change [J]
v, v	filtration velocity of hydrogen [m/s]
$\bar{d}V_{(c)}$	continuum volume element [$m^3_{(c)}$]
x	H-concentration [kmole$_H$/kmole$_{hyd}$].

Greek symbols

$\dot{\Theta}$	reaction rate
$\dot{\varphi}$	source/sink term [$kg_{H_2}/s \cdot m^3_{(c)}$]
μ	dynamic viscosity [kg/m·s]
ξ_0	hydride particle radius [m]
γ	molecular weight [kg/kmole]
ρ	density [kg/m^3]
ϕ	hydride matrix porosity [$m^3_{pore}/m^3_{(c)}$]
Π_2	dimensionless cooling potential
ϱ	particle density [particles$_{hyd}$/$m^3_{(c)}$]
Δ_{23}	regenerator efficiency
Δ_{45}	% refrigerator capacity used.

Superscript

$'$	refers to regenerator property.

Subscripts

b	binder
(c)	refers to continuum
a, d	absorption, desorption
f	fluid phase
hyd	hydride
n	time index
s	solid phase; surface
v	at constant volume
w	reactor wall.

spontaneous transpiration of H_2 to occur from the *refrigerator* (sub-phase $t_{4\to5}$). The enthalpy of desorption provides cooling; the concurrent enthalpy of absorption in the regenerator is rejected as rapidly as possible to sustain the driving potential.

Figure 2(a, b) shows an actual reactor and its schematic. The effective thermal conductivity of MH powders is insufficient for fast reactors [26] and powder beds quickly self-densify, limiting the permeability. In Fig. 2(a) the hydride is in the form of encapsulated particles in a sintered cylindrical porous matrix. For a two-component matrix five parameters specify the properties, ρ_{hyd}, ρ_b, ϕ, f, and ξ_0, and lead to the concept of the local particle density:

$$\varrho = \frac{n}{V}, \quad (\text{particles}_{hyd}/m^3_{(c)})$$

$$= \frac{1}{\frac{4}{3}\pi\xi_0^3} \frac{1-\phi}{\left[1+\left(\frac{\rho_{hyd}}{\rho_b}\right)\left(\frac{f}{1-f}\right)\right]} \quad (2)$$

(which will be referred to in Section 3) and the thermal waste fraction $F_Q = [f/(1-f)] \cdot c_{p_b}/c_{p_{hyd}}$. The design of an MH reactor begins by comparing internal reactor processes to the ability of the *containment* to transfer heat. Doing so results in two dimensionless parameters [18]:

$$\Pi_2 = \frac{\text{energy transfered from the reactor}}{\text{thermal energy stored by the reactor}}$$

$$= (A_w)\left(\frac{\Delta T}{\frac{1}{h_c}+\frac{1}{h_\infty}+\frac{L}{k_w}}\right)\left(\frac{\Delta t}{\Delta U}\right) \quad (3a)$$

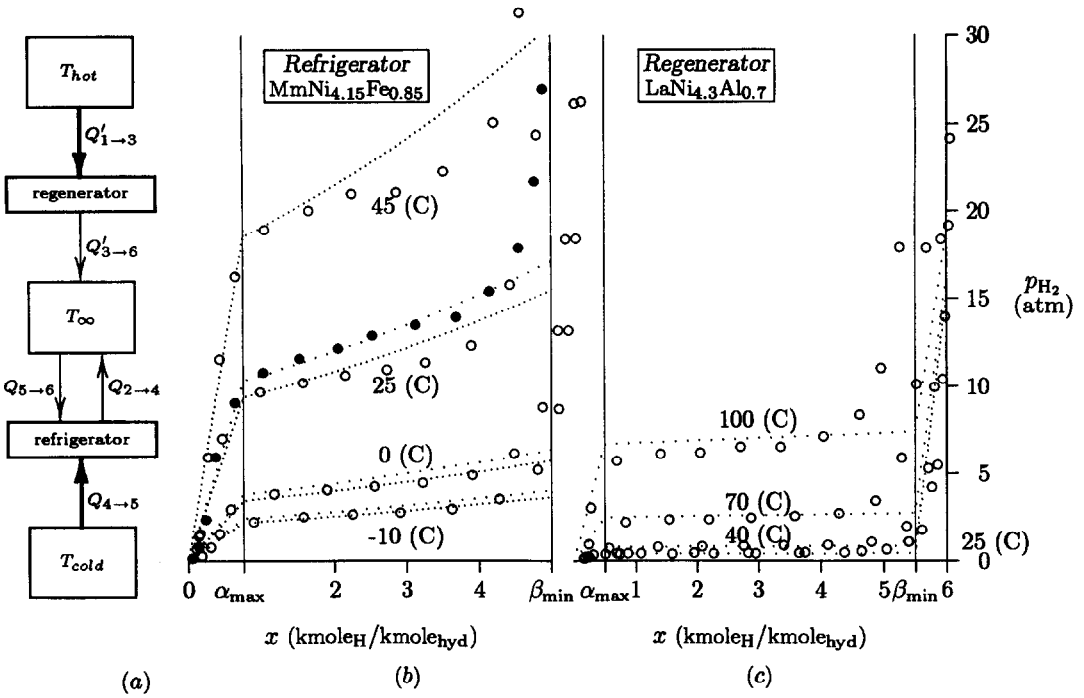

Fig. 1. (a) System diagram. (b) and (c): selected isotherms of p_{eq} vs concentration. Curve fits are shown with dotted lines. '○' and '●' denote data for desorption and absorption, respectively.

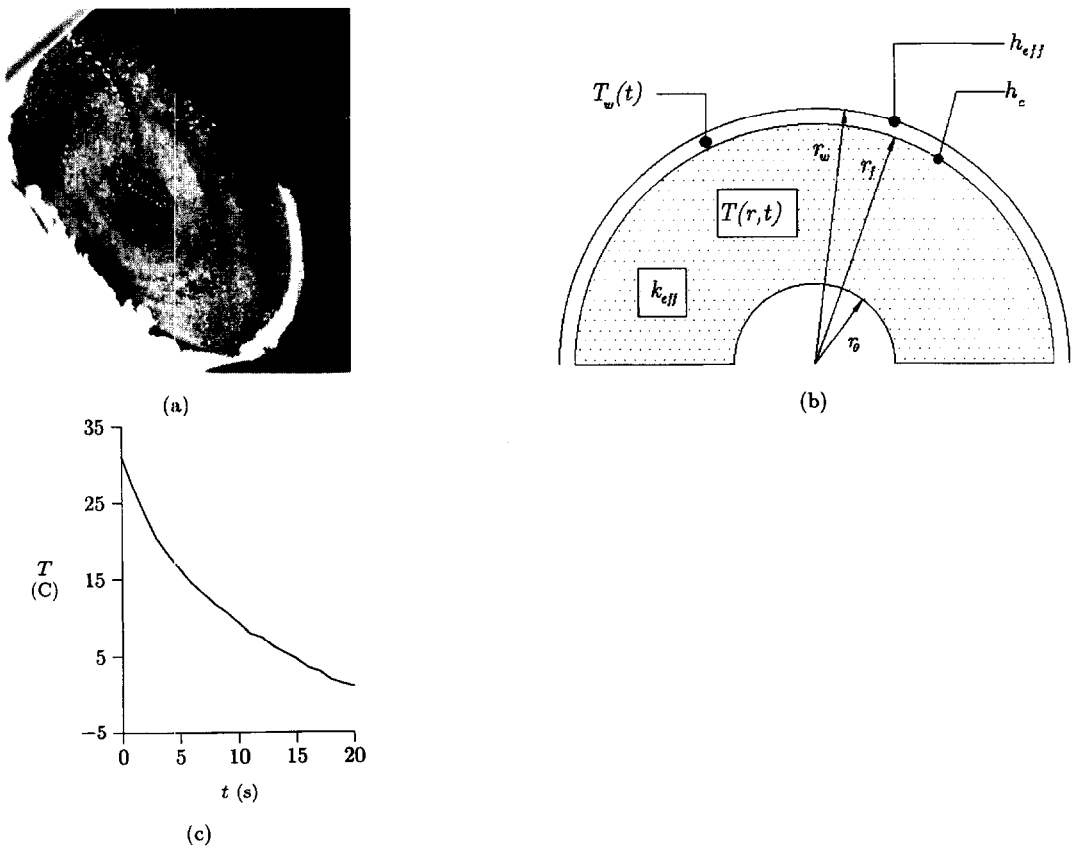

Fig. 2. (a) Cross-section of reactor using $LaNi_5$; (b) one-dimensional approximation; (c) external temperature history (vertical free convection) at a suction pressure of $\approx 10^{-3}$ torr.

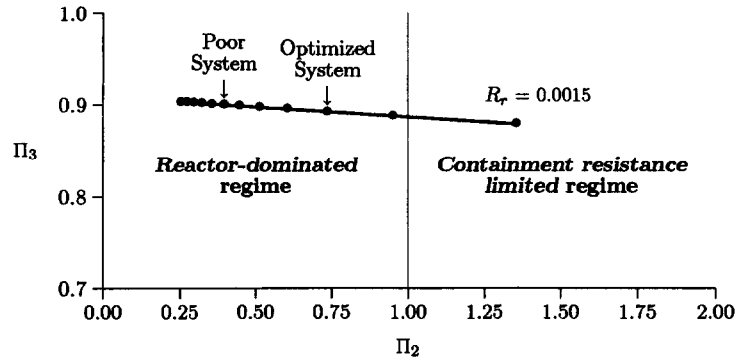

Fig. 3. The potential cooling (after parasitic thermal losses) vs the maximum possible energy transferable through the containment thermal resistance, R_r. The line is parameterized by $r_f - r_0$. This paper examines what happens as the arrow is moved to the right. $\Delta t = 75$ s, $\Delta T = 20°C$.

$$\Pi_3 = \frac{\text{available cooling energy}}{\text{theoretical cooling energy}} = \frac{\Delta U - \Delta U_{hyd} - \Delta U_b - \Delta U_w}{\Delta U}. \quad (3b)$$

The term ΔU is the energy change between two states with Δt and ΔT specified as design parameters. The term $1/h_c + 1/h_\infty + L/k_w$ is *defined* as the thermal containment resistance, R_r and its value determines the operating regime of a reactor regardless of any particular cycle. For simplicity studies are frequently limited to planar geometries. Cylindrical reactors are more suitable for fabrication and in this case $\Pi_2 \sim 2/r$.

Equation (3b) provides a scale for thermal losses arising from $c_{p_{hyd}}$ itself, of the inert matrix fraction and of the reactor shell. Larger values of r reflect favorably on this parameter. This has been noted, but the attendant disadvantage on Π_2 discussed above has not been emphasized [27]. Π_3 is plotted against Π_2 in Fig. 3 for a *specific* value of R_r corresponding to the value that will be used in the sequel. It should be noted that in equation (3b) the parasitic mass of specific heat exchanger devices is not included. Without careful consideration of this issue the slope of the parameterized curve in Fig. 3 can become more negative, considerably complicating optimization. The terms *reactor-dominated* and *containment-limited* will be clarified in Section 6.

3. FORMULATION

The governing equations are derived by considering a stationary control volume of the porous continuum. Local thermodynamic equilibrium between solid and fluid phases $(T_s - T_f)h_{sf}\,dA_s/dV_{(c)} \approx 0$ is assumed [28]. The energy balance becomes [25, 29]:

$$k_{eff}\nabla^2 T - \underline{\nabla}\cdot(\rho_f c_{p_f} T\underline{v}) + g = \frac{\partial[(1-\phi)\rho_s c_{v_s} T + \phi\rho_f c_{v_f} T]}{\partial t} (J/m^3_{(c)}\cdot s). \quad (4)$$

The first term incorporates the Fourier conduction flux (with $k_{eff} = [(1-\phi)k_s + \phi k_f]$ the stagnant thermal conductivity) and the second term advection of sensible heat by the fluid phase as well as the pv work done on the control volume. The source term g is the thermal energy released due to the change in enthalpy of a large number of particles. Equation (4) does not account for dispersion phenomena. The numerical model will be limited to one-dimensional (1-D) (radial effects predominating) in which these can be neglected. The continuity equation for the fluid phase is given by:

$$-\underline{\nabla}\cdot(\underline{v}\rho_f) + \dot{\phi} = \phi\frac{\partial\rho_f}{\partial t}(kg_{H_2}/m^3_{(c)}\cdot s). \quad (5)$$

The source term $\dot{\phi}$ represents the absorption-/desorption effect for the fluid phase. The ideal gas equation of state, $\rho_f \bar{R}T = p\gamma_{H_2}$, may be used for H_2. The proper momentum equation for the fluid phase is problematical. For the reactants used by the authors consideration of the particle Reynold's number, $Re_p = v\rho L_p/\mu = vp\gamma L_p/(T\bar{R}\mu)$ (with L_p taken as the Brinkman screening distance, $\sqrt{K}$), indicates that Darcy's law may be applied [18]:

$$v(r,t) = -\frac{K}{\mu}\frac{\partial p(r,t)}{\partial r}. \quad (6)$$

The term $\dot{\phi}$ is written in terms of the fundamental particle reaction rates, $\dot{\Theta}_a \overset{def}{=} \dot{x}_{\alpha\to\beta}$ and $\dot{\Theta}_d \overset{def}{=} \dot{x}_{\beta\to\alpha}$ using equation (2):

$$\dot{\phi}(kg_{H_2}/s\cdot m^3_{(c)}) = \begin{cases} -\frac{N_0}{2}\dot{\Theta}_a\left(\frac{kmole_{H_2}}{s\cdot particle_{hyd}}\right)\times\gamma_{H_2}\left(\frac{kg_{H_2}}{kmole_{H_2}}\right) \\ \qquad\times\varrho\left(\frac{particles_{hyd}}{m^3_{(c)}}\right) \\ -\frac{N_0}{2}\dot{\Theta}_d\left(\frac{kmole_{H_2}}{s\cdot particle_{hyd}}\right)\times\gamma_{H_2}\left(\frac{kg_{H_2}}{kmole_{H_2}}\right) \\ \qquad\times\varrho\left(\frac{particles_{hyd}}{m^3_{(c)}}\right) \end{cases} \quad (7)$$

where the negative sign reconciles a negative reaction

rate (desorption) with the proper sign for a source term. Similarly, the heat generation rate is:

$$g\left(\mathrm{J/s\cdot m^3_{(c)}}\right) = \begin{cases} \dfrac{N_0}{2}\dot{\Theta}_a\left(\dfrac{\mathrm{kmole_{H_2}}}{\mathrm{s\cdot particle_{hyd}}}\right)\times|\Delta H|\left(\dfrac{\mathrm{J}}{\mathrm{kmole_{H_2}}}\right) \\ \qquad\times\varrho\left(\dfrac{\mathrm{particles_{hyd}}}{\mathrm{m^3_{(c)}}}\right) \\ \dfrac{N_0}{2}\dot{\Theta}_d\left(\dfrac{\mathrm{kmole_{H_2}}}{\mathrm{s\cdot particle_{hyd}}}\right)\times|\Delta H|\left(\dfrac{\mathrm{J}}{\mathrm{kmole_{H_2}}}\right) \\ \qquad\times\varrho\left(\dfrac{\mathrm{particles_{hyd}}}{\mathrm{m^3_{(c)}}}\right) \end{cases} \quad (8)$$

Note that absorption (positive reaction rate) represents an energy source term for an exothermic reaction. The magnitude of this term can be very large indeed as inferred from Fig. 2(c).

The boundary conditions are derived elsewhere [25]. When coupled they are:

(coupling of pressure field) $$p(r_{0'},t)=p(r_0,t) \quad (9a)$$

(conservation of mass) $$\left(\frac{K'}{K}\right)\frac{1}{T(r_{0'},t)}\frac{\partial p(r_{0'},t)}{\partial r}\frac{A_{0'}}{A_0} = -\frac{1}{T(r_0,t)}\frac{\partial p(r_0,t)}{\partial r} \quad (9b)$$

$$\begin{pmatrix} t\in t_{2\to3}, \text{conservation of advected} \\ \text{energy for transpiration} \\ \textit{to} \text{ refrigerator } \textit{from} \text{ regenerator} \end{pmatrix}$$

$$\begin{cases} \dfrac{\partial T(r_0,t)}{\partial r}A_0 = -\left(\dfrac{c_p\gamma K'}{k\bar{R}\mu}\right) \\ \times\dfrac{p(r_{0'},t)}{T(r_{0'},t)}\dfrac{\partial p(r_{0'},t)}{\partial r}[T(r_{0'},t)-T(r_0,t)]A_{0'} \\ \dfrac{\partial T(r_{0'},t)}{\partial r}=0 \end{cases} \quad (9c)$$

$$\begin{pmatrix} t\in t_{4\to5}, \text{conservation of advected} \\ \text{energy for transpiration} \\ \textit{from} \text{ refrigerator } \textit{to} \text{ regenerator} \end{pmatrix}$$

$$\begin{cases} \dfrac{\partial T(r_{0'},t)}{\partial r}A_{0'} = -\left(\dfrac{c_p\gamma K}{k'\bar{R}\mu}\right) \\ \times\dfrac{p(r_0,t)}{T(r_0,t)}\dfrac{\partial p(r_0,t)}{\partial r}[T(r_0,t)-T(r_{0'},t)]A_0 \\ \dfrac{\partial T(r_0,t)}{\partial r}=0 \end{cases} \quad (9d)$$

When the reactors are uncoupled the boundary conditions are reasonably approximated as zero gradient constraints on T and p (if the artery radius is small).

4. NUMERICAL SOLUTION

Equations (4) and (5) are coupled to local kinetic rate equations. Together there are eight primary variables: the temperature in four domains (when the reactor wall is included) and the pressure and concentration in two domains. The initial conditions are known. The boundary conditions are well-posed, though time-varying and complex. A finite-difference approximation was deemed appropriate to integrate the system. An explicit method was chosen to deal directly with the nonlinear terms. It can be shown that the coupled PDEs are linear in the discretized time-derivatives of T and p, making this approach particularly convenient. Finite-difference approximations $\mathcal{O}(\Delta r)^2+\mathcal{O}(t)$ were developed for all node points. The continuity equation (5) in cylindrical coordinates is given by:

$$\left(\frac{K\gamma}{\bar{R}\mu}\right)\left\{p\frac{\partial^2 p}{\partial r^2}+\frac{\partial p}{\partial r}\left[\frac{p}{r}+\frac{\partial p}{\partial r}-\frac{p}{T}\frac{\partial T}{\partial r}\right]\right\}+\phi\dot{T} = \left(\frac{\phi\gamma}{\bar{R}}\right)\left[\frac{\partial p}{\partial t}-\frac{p}{T}\frac{\partial T}{\partial t}\right] \quad (10)$$

the energy equation is

$$k_{\mathrm{eff}}\left[\frac{\partial^2 T}{\partial r^2}+\frac{1}{r}\frac{\partial T}{\partial r}\right]+\left(\frac{Kc_{p_f}\gamma}{\bar{R}\mu}\right)\times\left[p\frac{\partial^2 p}{\partial r^2}+\left(\frac{\partial p}{\partial r}\right)^2+\frac{p}{r}\frac{\partial p}{\partial r}\right]+g = (1-\phi)\rho_s c_{v_s}\frac{\partial T}{\partial t}+\left(\frac{\phi c_{v_f}\gamma_{H_2}}{\bar{R}}\right)\frac{\partial p}{\partial t}. \quad (11)$$

The discretization method is described in [25, 30–32]. For conciseness let $y_i^n=\langle p_i^n, T_i^n\rangle^{\mathrm{T}}$ represent the solution at the discrete time $n\Delta t$ at the node i. For a given node i or i' the discretized continuity and the energy equations may be written as linear, inhomogeneous algebraic equations $\underline{A}\underline{y}_i^{n+1}=\underline{C}(\underline{y}_i^n)$, where $\underline{A}$ and $\underline{C}$ are functions of n [25]. The explicit formula for the solution at each node i or i' follows: $\underline{y}_i^{n+1}=\underline{A}_i^{-1}\underline{C}_i$; this is the goal of any finite difference scheme [33]. A number of procedures were used to check stability, convergence, and overall satisfaction of integral balance laws [25].

Equation (3a) indicates that regardless of the wall composition internal gradients can be ignored. A suitable discretization in this case is:

$$T_w^{n+1}=T_w^n\left[1-2\Delta t\frac{r_f h_c+r_w h_\infty(t)}{\rho_w c_{p_w}(r_w^2-r_f^2)}\right]+2\Delta t\left[\frac{r_f h_c T_N^n+r_w h_\infty(t)T_{\mathrm{reservoir}}(t)}{\rho_w c_{p_w}(r_w^2-r_f^2)}\right]. \quad (12)$$

Because of their importance the discretized boundary conditions during the coupled periods are derived here. Consider $t_{4\to5}$. On the refrigerator side (i.e. *transpiring side*), the adiabatic (no flux) condition on temperature automatically gives $T_1^n = (4/3)T_2^n - (1/3)T_3^n$ and from equation (9a) $p_1^n = p_{1'}^n$. Equation (9b) is solved for $p_{1'}^n$ and substituted into this to give:

$$p_1^n = \frac{a_1 + a_2 a_3 T_{1'}^n}{1 + a_2 T_{1'}^n} \tag{13}$$

where a_1, a_2 and a_3 are obtained straightforwardly. On the injection side, the *energy* coupling equation is solved for $T_{1'}^n$: $T_{1'}^n[a_4 p_1^n(a_3 - p_1^n) + 1] = a_5 p_1^n(a_3 - p_1^n) + a_6$, where a_4, a_5 and a_6 are obtained similarly. Solving for $T_{1'}^n$:

$$T_{1'}^n = \frac{a_3 a_5 p_1^n - a_5 (p_1^n)^2 + a_6}{a_3 a_4 p_1^n - a_4 (p_1^n)^2 + 1}. \tag{14}$$

Equation (13) is now substituted into this to give an expression containing only $T_{1'}^n$:

$$0 = \frac{(T_{1'}^n)^3 A + (T_{1'}^n)^2 B + (T_{1'}^n) C + D}{(T_{1'}^n)^2 E + (T_{1'}^n) F + G} \tag{15}$$

where A through G are obtained straightforwardly. Newton's method is used to find the zero of equation (15). Once $T_{1'}^n$ is found satisfying equation (15), p_1^n may be determined from equation (13). Automatically $p_{1'}^n = p_1^n$. For $t_{2\to3}$ the boundary conditions are obtained by interchanging the primed and unprimed indices above.

5. OVERVIEW

In order to relate transient heat and mass transfer processes to integral performance over a cycle Π_2 was chosen as the key optimization parameter. Five calculations were run in order to investigate the correspondence between Fig. 3 and the numerical results of the formulation presented in Sections 3 and 4. This section describes the calculations and discusses some aspects of the general reactor dynamics prior to examining them in detail in Section 6.

The MHs $LaNi_{4.7}Al_{0.3}$ and $MmNi_{4.15}Fe_{0.85}$ (Fig. 1) were chosen because of previous experimental work [34] as well as availability of data [11]. The reservoir temperatures were $T_\infty = 20$ (°C), $T_{hot} = 150$ (°C), and $T_{cold} = 0$ (°C). These represent reasonable values for many engineering applications. The boundary conditions included a "thermal switch" during $t_{4\to5}$ which reduced h_∞ between the refrigerator and the cold reservoir (to the small value 10 (W/m^2·K)) until the time at which the refrigerator reactor *wall* temperature fell below T_{cold}.

The heat capacities of both hydrides were 418.6 (J/kg·K) and for the system analysis pursued here taken as constant. The porosity was $\phi = 0.15$. A hydride density of 8000 (kg/m^3) was used which resulted in a bulk density of 6000 (kg/m^3); this is very close to the green densities of the reactants shown in Fig. 2(a). A value of $F_Q = 0.44$ characterized the reactant. The value of h_c depends upon the reactor fabrication process; little specific data is available. Values larger than 1000 (W/m^2·K) (the values used here) reportedly require exotic techniques [35]. The maximum external heat transfer coefficient h_∞ depends on the particular system configuration. Design issues related to h_∞ are of considerable importance in so far as thermal capacity degrades performance and introduces thermal lags [36]. A value of 2000 (W/m^2·°C) was used, resulting in $R_r = 0.0015$ (as noted in Fig. 3). The transport properties $K = 5 \times 10^{-15}$ (m^2) and $k_{eff} = 5$ (W/m·K) represent nominal values attainable using the materials preparation processes of the authors and which previous studies have shown represent the range where further optimization in these properties is counterproductive against efforts devoted toward increasing h_c and, in general, reducing R_r and F_Q.

The kinetic rate equation used for both absorption and desorption is:

$$\frac{dx}{dt} = A\, e^{-E_a/\bar{R}T} \ln\left(\frac{p}{p_{eq}}\right). \tag{16}$$

Values of the activation energies for $MmNi_{4.5}Al_{0.5}$ ranging between 22.8×10^6 (J/kmole$_{H_2}$) to 60.2×10^6 (J/kmole$_{H_2}$) were reported in [37]. The present study used a value of 30×10^6 (J/kmole$_{H_2}$) for both hydrides. It is difficult to discern values of A, the reaction prefactor, for what the authors term the intrinsic particle kinetics. Parametric studies indicated that values between 10^4 and 10^5 controlled the initial transient period without affecting the following regime. Lower values of A noticeably affected this regime. Based upon these studies and correlating the transient phase with laboratory experiments a value of 10^5 was used for both hydrides.

As noted in Section 2 equilibrium MH behavior deviates considerably from ideal Gibbsian behavior. The hysteretic behavior has been attributed to irreversible (though repeatable) deformation effects [38, 39]. For realistic simulations both the plateau slope and hysteresis must be incorporated and the approximation must be fast and invertible. The van't Hoff equation was modified within the plateau region with linear corrections. For $x \in [x_{\alpha_{max}}, x_{\beta_{min}}]$:

$$\ln p_{eq_{H_2}} = \frac{\Delta H}{\bar{R}T} - \frac{\Delta S}{\bar{R}} + \Delta \ln p_x \cdot \left(\frac{x - x_{\alpha_{max}}}{x_{\beta_{min}} - x_{\alpha_{max}}}\right) + \begin{cases} \ln\left(\dfrac{p_a}{p_d}\right) & \text{absorption} \\ 0 & \text{desorption} \end{cases} \tag{17}$$

was fitted to equilibrium data in the literature. The plateau limits [Fig. 1(b, c)] were taken as constant. Outside the plateau region (in the α and β single-

phase regions) the isotherms are fitted by the simplest possible technique—straight lines. However, this work assumes the reaction rate ceases whenever the boundary concentrations of the plateau region are approached. Because of the lack of hysteresis scans in the plateau region the model sets the reaction rate to zero. The MH parameters used were: $MmNi_{4.15}Fe_{0.85}$: $\Delta H = -2.68 \times 10^7$ (J/kmole$_{H_2}$); $\Delta S = -1.085 \times 10^5$ (J/kmole$_{H_2}$·K); $\Delta \ln p_x = 0.5$; and $\ln(p_{eq_a}/p_{eq_d}) = 0.1$. $LaNi_{4.7}Al_{0.3}$: $\Delta H = -3.47 \times 10^7$ (J/kmole$_{H_2}$); $\Delta S = -1.088 \times 10^5$ (J/kmole$_{H_2}$·K); $\Delta \ln p_x = 0.1$; and $\ln(p_{eq_a}/p_{eq_d}) = 0.1$.

The duration of the cycle was 250 (s) with the following breakdown of intermediate phases: *preheating*, $t_{1\to2} = 50$ (s); *charging*, $t_{2\to3} = 75$ (s); *equilibriation*, $t_{3\to4} = 25$ (s); *cooling*, $t_{4\to5} = 75$ (s); and *equilibriation*, $t_{5\to6} = 25$ (s). Figure 4(a, b) shows the field evolution for $\dot{\varphi}$ and x for what will be termed the *optimized system*, $\Pi_2 \approx 0.74$; Fig. 4(c, d) for the *poor system*. $\dot{\varphi}$ and x were chosen as the most descriptive field quantities to illustrate the general reactor dynamics. Note that the regenerator reactor is plotted with a negative radius. In Fig. 4 each plot contains both a three-dimensional (3-D) representation and a projection onto the r–t plane. The 3-D visualization is useful in identifying transient peaks and spatial gradients; the projections more clearly show the reaction fronts.

A brief description of the cycle is appropriate at this point. The *preheating* phase causes rapid redistribution of the absorbed H_2 within the regenerator. No changes occur in the refrigerator during this period. During the *charging* phase the reactors are coupled with H_2 at high temperature and pressure transpiring from the regenerator into the refrigerator where it is absorbed. During the subsequent phase $t_{3\to4}$ the reactors are isolated and each rapidly brought near T_∞ in order to establish the largest equilibrium desorption potential possible. This is necessary, since the lower average reactors temperatures during the coupled *cooling* phase $t_{4\to5}$ slow the kinetics via the Arrhenius behavior associated with equation (16). During this phase hydrogen transfers to the regenerator. The H_2 transpiring from the refrigerator cools the regenerator and establishes an absorption front which propagates outward from the core. The rapid elimination of the enthalpy of absorption at the regenerator wall favors an inward absorption front. The combined effects give rise to the central depletion region readily observed in Fig. 4(b, d). The hydrogen transfers during the coupled phases are summarized

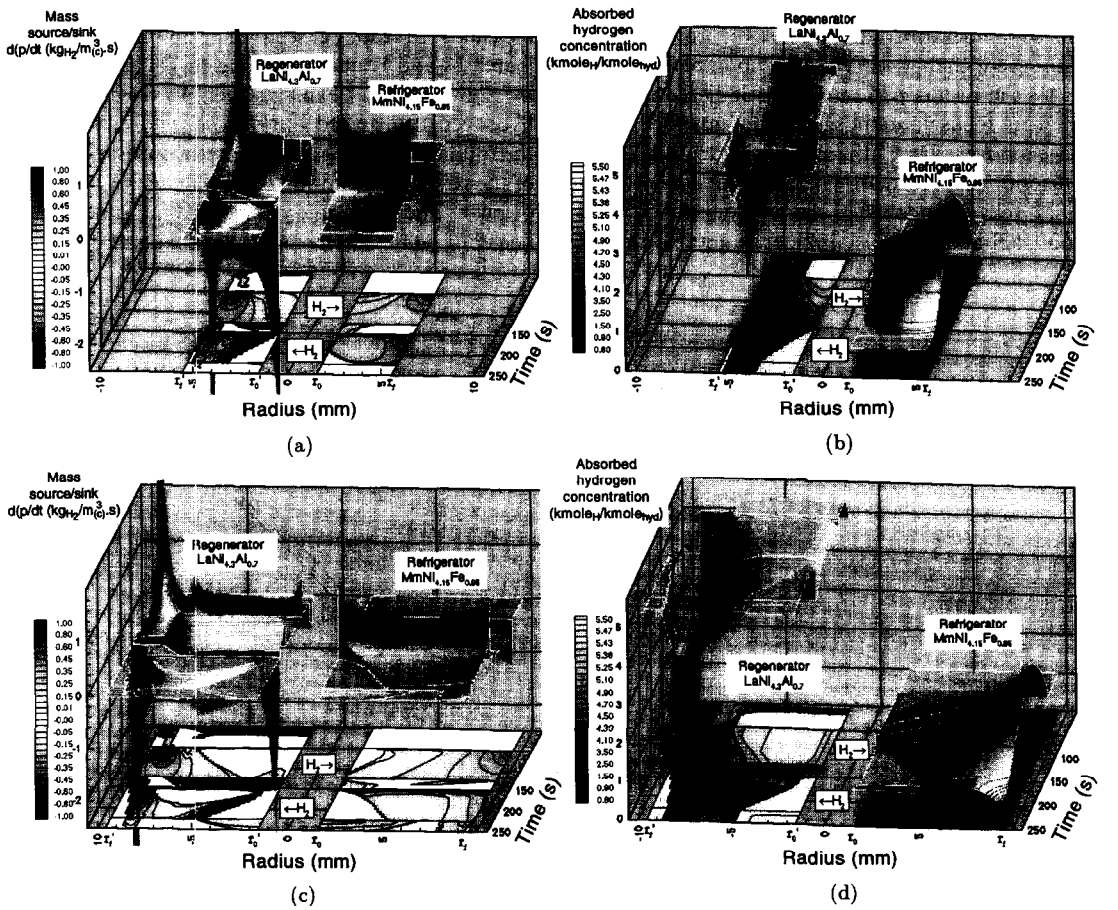

Fig. 4. Optimized system: (a) evolution of $\dot{\varphi}$ absorption/desorption term; (b) absorbed hydrogen concentration x. Poor system: (c) $\dot{\varphi}$; (d) x (from calculation data sampled at 1 s increments).

Table 1. Summary of calculations

Π_2	$r_f - r_0$ (mm)	Δr (mm)	m_{hyd} (kg)	m_b (kg)	$n'_0(50^-)$ ($mole_{H_2}$)	$\Delta n_{2\to3}$ ($mole_{H_2}$)	Δ_{23}%	$n_0(150^-)$ ($mole_{H_2}$)	$\Delta n_{4\to5}$ ($mole_{H_2}$)	Δ_{45}%
0.74	4	0.20	0.05681	0.01164	0.33367	−0.10122	−33.8	0.17015	−0.12018	42.7
0.60	5	0.20	0.08099	0.01659	0.47627	−0.12189	−28.5	0.21970	−0.14359	35.8
0.51	6	0.24	0.10915	0.02236	0.64036	−0.14064	−24.5	0.27358	−0.16360	30.2
0.45	7	0.28	0.14131	0.02894	0.82924	−0.15926	−21.4	0.33142	−0.18339	26.2
0.40	8	0.20	0.17745	0.03635	1.04938	−0.18225	−19.2	0.39252	−0.20228	23.0

in Table 1. Δ_{23} is the fraction of regenerator precharge transferred to the refrigerator during the preheating phase. Δ_{45} is the fraction of hydrogen transferred during the cooling phase relative to the theoretical maximum value. Table 1 indicates that hydride utilization rises significantly as Π_2 increases.

The large variations in T and p over the cycle and the rapid transients which occur when the reactors are coupled make it productive to examine the process paths in Fig. 5. The field point selected is at $r = 2.75$ mm, distant from the wall reaction fronts, but situated in the outward absorption front during $t_{4\to5}$. As the point is near the core it is notable that the regenerator of the optimized system more closely approaches T_{hot} prior to $t_{2\to3}$, thus establishing a higher potential for charging the refrigerator. In any case, Fig. 5 shows that the regenerator undergoes much more pronounced temperature fluctuations. Figure 4(b, d) also shows severe changes in x. Based upon recent studies [40, 41] the results presented here indicate that MH refinement focus upon those hydrides intended for use as regenerators. The paths also illustrate quite clearly the reaction front formation regime that occurs during the first few seconds when the reactors are coupled: $t \in [50^+, 52]$ and $t \in [150^+, 152]$. It is notable that the injection of cold H_2 during the stabilized cooling regime results in the complicated regenerator process shown.

Figure 6 shows the final performance data obtained from all five calculations as the "arrow" in Fig. 3 is moved into the containment resistance limited regime. The dependent variables were calculated as follows:

$$\mathrm{COP} = \frac{Q_{4\to5}}{Q'_{1\to2} + Q'_{2\to3}} \tag{18}$$

$$P = \frac{Q_{4\to5}}{t_{4\to5} \cdot m_{hyd}} \quad (\mathrm{W/kg_{hyd}}) \text{ at } T_{cold}$$

where the Qs are the heat transfers through the reactor boundaries and m_{hyd} for the refrigerator is used. The graph is essentially linear in Π_2 for both performance measures. It can be seen that power dramatically increases and is quite sensitive to Π_2 as "predicted" by Fig. 3. Table 1 explains this. As Π_2 increases the hydrogen transferred during *charging* increases and the total utilization of the theoretical storage capacity of the refrigerator during *cooling* increases by a factor of two. The reactor dynamics responsible for this behavior will be discussed in the next section.

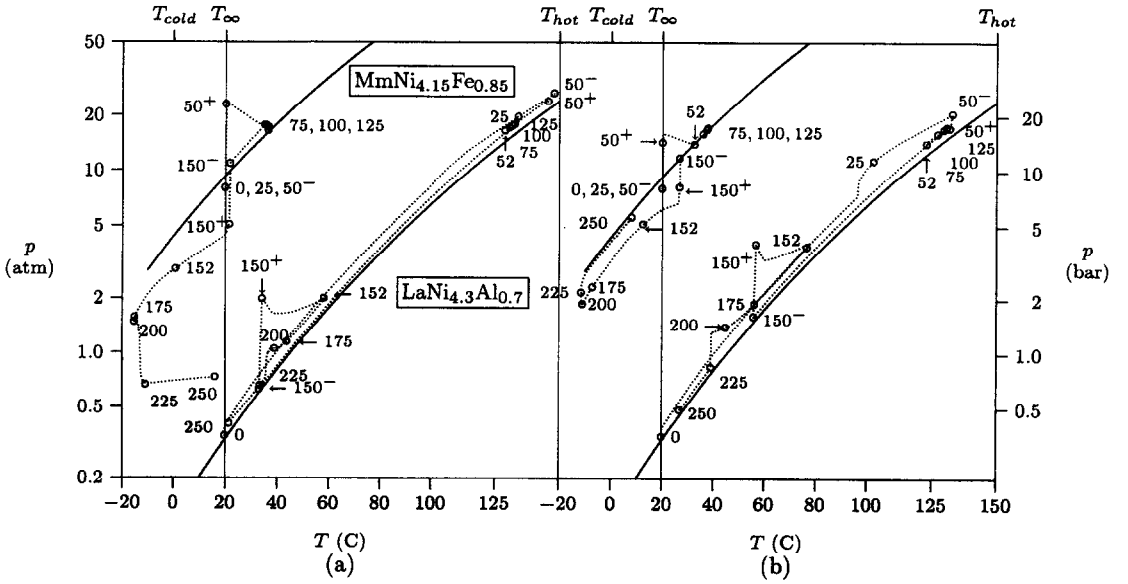

Fig. 5. (a) Optimized system; (b) poor system. Process paths at $r = 2.75$ mm. The solid lines are the ideal van't Hoff behavior. The dotted lines are the LTE temperature and pore pressure parameterized over t for the complete cycle. Selected times of interest are indicated.

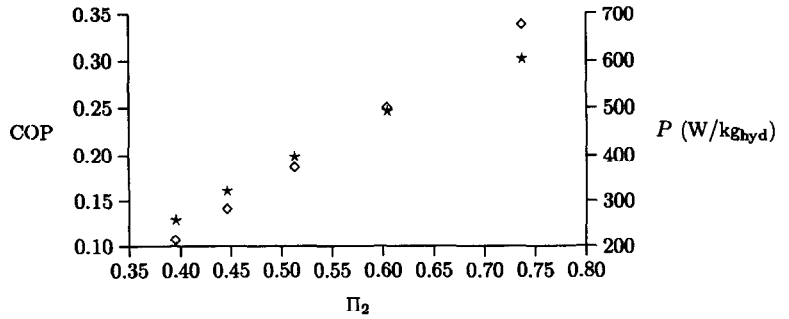

Fig. 6. COP, ★, and average cooling power P, ◇, as a function of the optimization parameter Π_2.

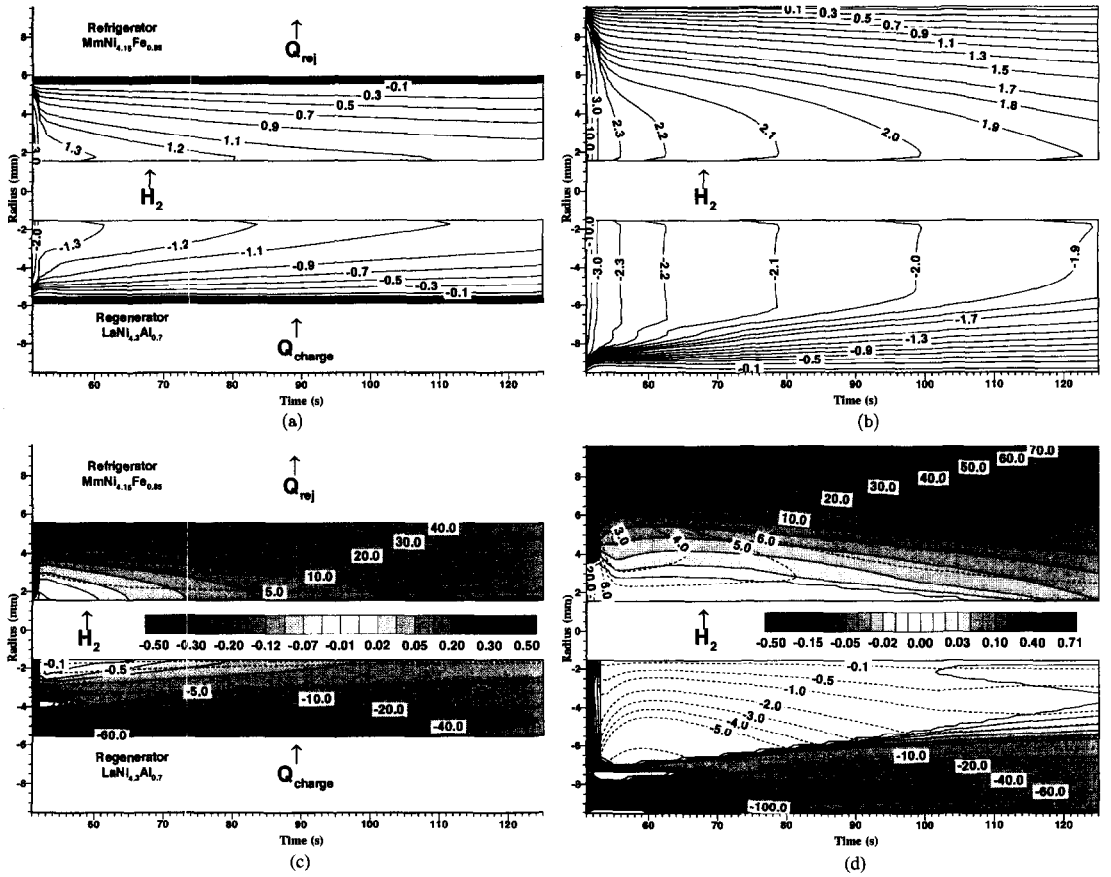

Fig. 7. (a) Optimized system; (b) poor system. Contours of H_2 [(mole$_{H_2}$/s) $\times 10^3$] transport in the coupled reactors during the phase $t_{2\to3}$; (c) optimized system; (d) poor system. Flooded contours of $\dot{\phi}$ (kg$_{H_2}$/m$^3_{(c)}$ · s) and conduction energy transport (dashed contours) (J/s) during $t_{2\to3}$.

6. DISCUSSION OF TRANSIENT BEHAVIOR

We consider the coupled phases $t_{2\to3}$ and $t_{4\to5}$. Figures 4 and 5 illustrate the behavior for the other phases. Table 1 confirms the correspondence between net transfer of H_2 and power and COP in accordance with basic thermodynamic considerations. Given the deviations from equilibrium evident in Fig. 5 it is reasonable to ask what processes predominate.

The transport contour plots (in which molar flux has been multiplied by area in order to eliminate the effect of geometry) in Fig. 7(a, b) compare the extreme cases of Π_2 for the charging phase. They begin to illustrate the connection between the integral results in Table 1 and the reactor dynamics. Specifically, the *optimized system* ($\Pi_2 \approx 0.8$) reveals a rising pickup front extending over the entire bed progressively increasing in magnitude and directed inward from the energy input surface. In contrast the *poor system* ($\Pi_2 \approx 0.4$) shows the pickup front confined near the reactor wall. In both systems Fig. 7 shows a large initial peak followed by a slowly declining "flow-stabilized" regime. The duration of the peak is longer for the poor system.

Further explanation can be obtained from Fig. 7(c, d). These show flooded contours of $\dot{\phi}$; the dashed contours indicate conduction energy transport. The behavior of the pickup fronts in Fig. 7(a, b) in the regenerators are explained by these desorption fields. The first few seconds following coupling are characterized by high rates of desorption throughout the entire bed (simply because the thermochemical potentials previously established are sufficiently homogeneous). Once the pressure gradients have dissipated the average regenerator temperature has dropped several degrees (Fig. 5) and the predominate nature of the charging phase (with the regenerator connected to the T_{hot} reservoir) is revealed—specifically a "steady-state" desorption front is established a few zones inward from the wall. The peak of the front remains confined near the wall. In both systems it broadens and declines with time. The conduction transport contours show the pronounced effect that g has on the nature of the energy transport in both regenerators. As thermal energy enters the reactor and crosses the depletion zone it initiates desorption. The rapid endothermic reaction accompanying the $\beta \rightarrow \alpha$ phase transition stops the conduction front and "shields" the inner region of the regenerators from the T_{hot} reservoir, despite its close proximity. On the basis of Fig. 7 it is reasonable to speak generally of a desorption front in the regenerator where the process of H_2 evolution and the endothermic phase transition accompanying local transpiration balances thermal conduction into the regenerator once the initial coupling transient, lasting but a few seconds, has concluded.

The development of the desorption front a few zones inward represents a coupling between x evolution and the conditions established during $t_{1\rightarrow 2}$; i.e. referring to Fig. 4(b, d) it is seen that the initially homogeneous concentration profile of the regenerator is drastically altered—hydrogen transpires from the reactor wall, advects inward and is absorbed. The uniform "hydration" zone idealization is thus an approximation for the regenerator. The regenerator in the poor system shows absence of any desorption near the core in spite of a declining pressure gradient and higher concentration. The core temperature is simply too low for desorption to commence. The poor system shows limited conduction transport in the nonreacting region. At early times this is due to advection of hot H_2 inward.

From an overall point of view it is important to examine the pronounced asymmetry between the dynamics of the refrigerator and regenerator. Hot H_2 injected into the refrigerator core suppresses absorption as evident in Fig. 7(c, d); any absorption which commences self-limits by the requirement that the heat of absorption be removed. Thermochemically absorption is favored at the refrigerator wall. However, as x increases the steep plateau slope diminishes this potential; the competing dynamic mechanisms of absorption and energy transport through the path of least resistance promote the much smoother reaction fields in the refrigerator.

The steep concentration gradients apparent in Fig. 4 and quantitatively shown in Fig. 8(a, b) illustrate the depletion region adjacent to the wall in the regenerator. In the poor system the charging phase *begins* with complete depletion at $x(r'_f) \approx x'_{a_{max}}$; in the kinetic model used no further desorption is possible. In contrast, $x(r_f, 50) = 1.8523$ $(\text{kmole}_H/\text{kmole}_{hyd})$. Despite the difference *at* the *boundary* the evolution of the desorption fronts is remarkably similar as shown in Fig. 8(c).

Figure 5 indicates that the temperature of the regenerator for both systems increases for $t \in [52, 125]$ (s). As the desorption front broadens and widens the average pore pressure increases in order to sustain the driving potential required for absorption in the refrigerator. In both reactors the initial cooldown period self-limits; continued heat transfer from the reservoir T_{hot} then causes the average regenerator temperature and hence pressure of both systems to rise. For the optimized system the average pressure increases about 1.2 bar; for the poor system about 3.1 bar. The rise in T and p for both systems implies that rejection of the heat of absorption in the *refrigerator* reactor is the overall limiting process during this phase. Since both hydrides have the same kinetic parameters the lower p and much lower T on average in the refrigerator provide the essential reason for this behavior.

The reactor dynamics during the cooling phase are considerably more complicated. When initially coupled the desorption gradient established during the prior phase $t_{3\rightarrow 4}$ rapidly transfers H_2 to the regenerator. This is illustrated in Fig. 9(a, b). Until the time when $T_w < T_{cold}$ (Fig. 9(c, d)) the refrigerator interacts only weakly with external reservoirs; the substantial conduction transport inward results from cooling the reactor wall. Figure 9(a, b) shows that the *cold* H_2 injected into the regenerator promotes an absorption front which moves outward from the core, in contrast to the behavior during $t_{2\rightarrow 3}$. Simultaneously, the rejection of the enthalpy of absorption at the regenerator wall promotes an inward moving absorption front. The key observation is that in the optimized system the available hydrogen is depleted within $t_{4\rightarrow 5}$ [at 223 (s)]. Figure 9(b) indicates that the poor refrigerator remains undepleted and sustains desorption. In the optimized system once the refrigerator has been depleted the regenerator maintains the inward progression of the absorption front at the expense of desorption near the regenerator core.

In both systems the regenerator region enclosed between converging absorption fronts is kinetically stagnant despite lower x. This island is barely discernable in the optimized system, but quite prominent in the poor system. This phenomena is due to the large ΔH associated with absorption. The outward moving front liberates heat which must be conducted through this region. Near the regenerator wall heat is easily

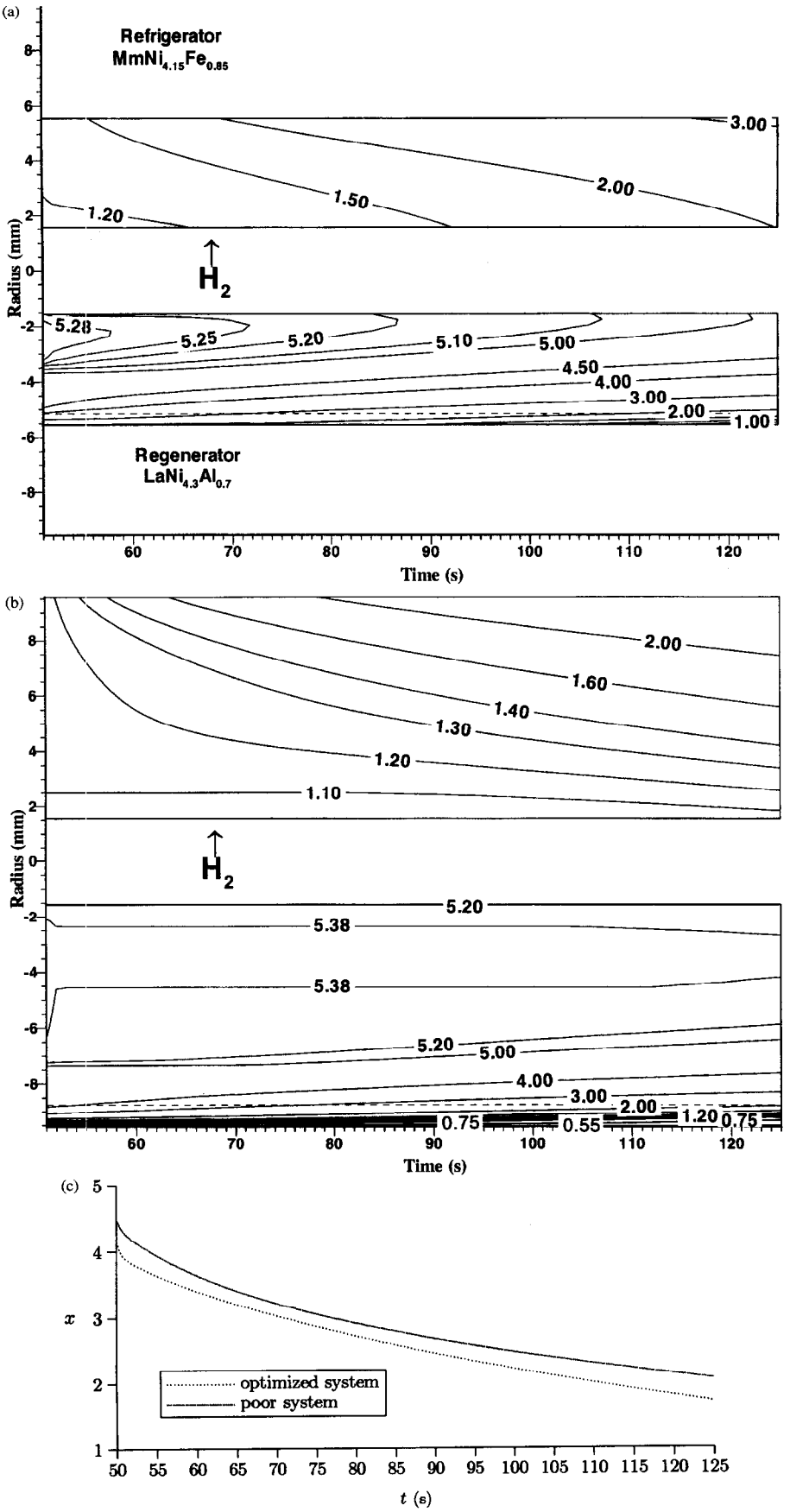

Fig. 8. (a) Optimized system; (b) poor system. Contours of absorbed hydrogen, x ($kmole_H/kmole_{hyd}$). The dashed line in the regenerators is the field point for the time histories in (c).

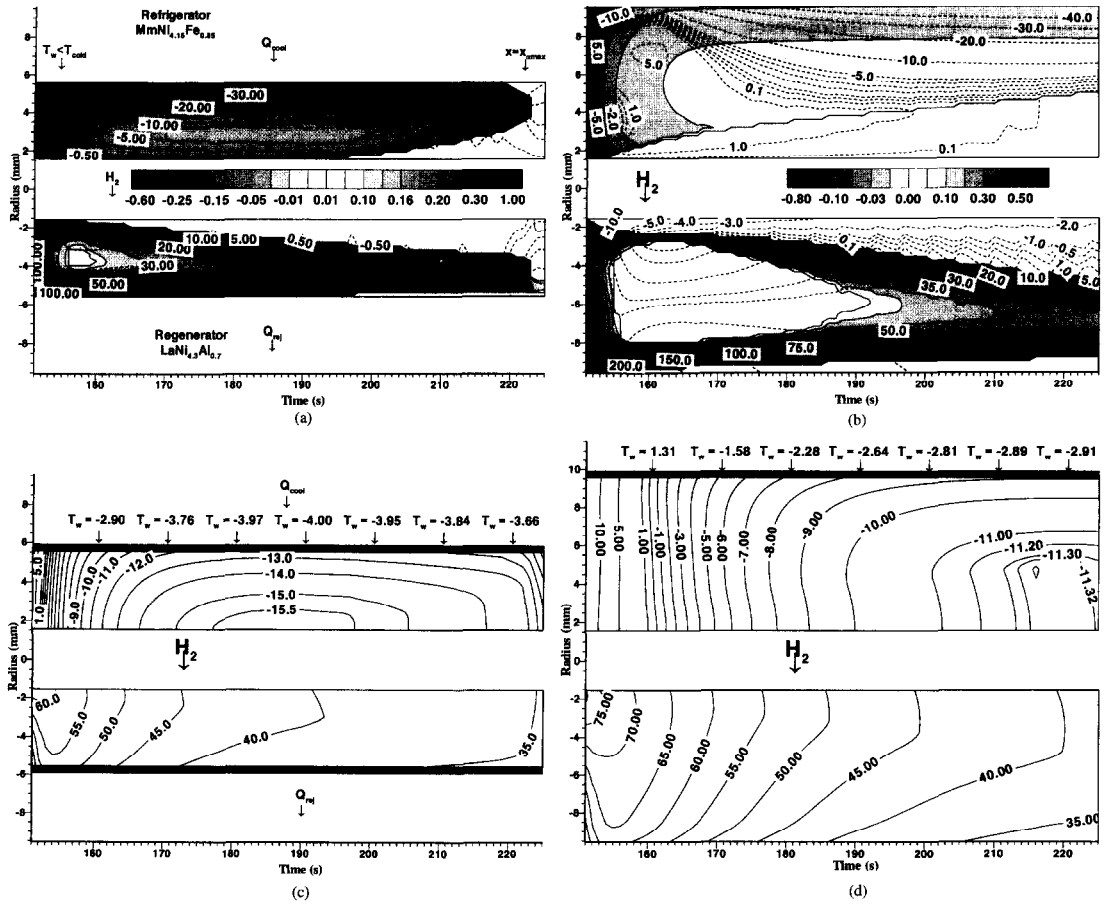

Fig. 9. (a) Optimized system; (b) poor system. Flooded contours of $\dot{\varphi}$ ($kg_{H_2}/m^3_{(c)} \cdot s$) and conduction energy transport (dashed contours) (J/s) during $t_{4\to5}$; (c) optimized system; (d) poor system. Temperature contours during $t_{4\to5}$.

liberated to the ambient reservoir, although the thermal path increases with time as complete absorption progresses inward.

Figure 9(c, d) shows the temperature field development. Several values of T_w are indicated; these show the substantial influence of h_c. Three observations can be made. First, the initial rate of cooling prior to $T_w < T_{cold}$ is extremely rapid and in accordance with experimental data [Fig. 2(c)]. Secondly, following this cooldown period the temperature field in the reactor is homogeneous until the rate of decrease of temperature falls and the limiting steady-state refrigerator temperature is achieved. This occurs *much earlier* in the optimized system along with a much lower average reactor temperature. This in part accounts for the high specific powers indicated in Fig. 6. Lastly, the interplay between p_{eq}, T, x in the refrigerator deserves to be mentioned. As this reactor becomes depleted the desorption gradient falls substantially. This is noted in Fig. 5. Specific cooling power P peaks in Fig. 9(c) at about 190 s. On the other hand, while P of Fig. 9(d) (the poor system) is much lower, it continues to increase with time.

It is interesting to examine the parameter arising from non-dimensionalizing equation (10): $Lr = \dot{\varphi}/(v\rho_f/\Delta r)$. Lr resembles Damköhler numbers [42, 43]. In a reacting porous flow Lr indicates the local thermochemical potential relative to the ability of the matrix to advect pore fluid. The *cell Lr* field is given in Fig. 10 for the cooling phase. Note that boundary regions where $v \to 0$ are not necessarily included. Lr at constant r in the transpiring refrigerator is remarkably constant for both systems in those regions where $\dot{\varphi} > 0$. This is particularly so even during the initial transient period and evidently values near unity clearly demarcate the reaction fronts.

The conclusion to be drawn is that the constant Lr through the initial transient (when $\dot{\varphi}$ is indeed large) into the stabilized regime indicates the transport parameter K is sufficient so that resistance to advection is minimal. Figure 3 indicates that the optimized system Fig. 10(a) is in the *containment-limited* regime. Yet, Fig. 3 does not consider K (nor k_{eff}). The sufficiency of the transport parameters (both K and k_{eff}) must be established by separate transient calculations [44] as well as the observation concerning Lr. That is, while

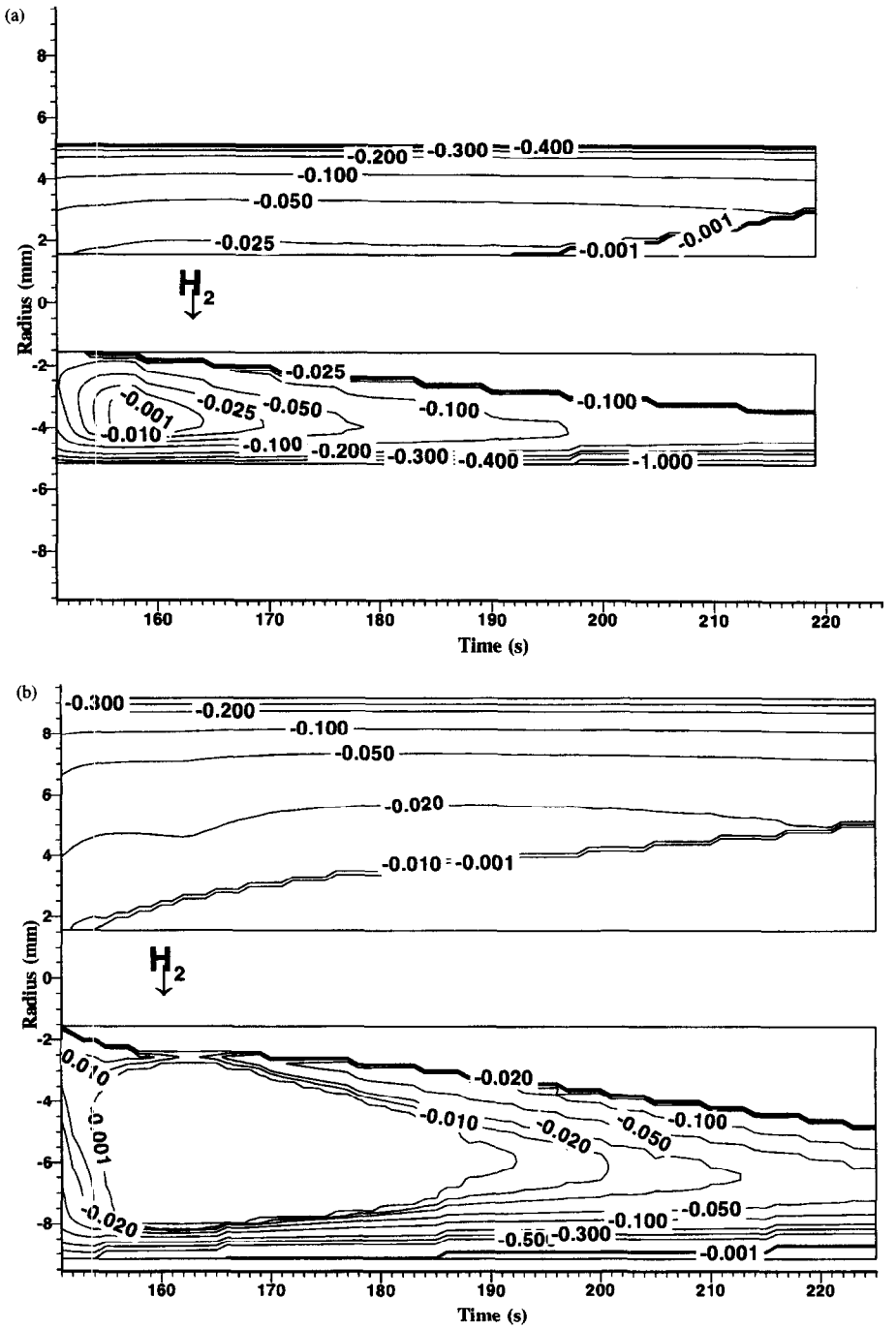

Fig. 10. (a) Optimized system; (b) poor system. *Lr* number during the cooling phase $t_{4\to5}$.

K and k_{eff} must be asymptotically large this does not necessarily guarantee containment-limited operation. If Π_2 is in what Fig. 3 terms the *reactor-dominated* regime geometrical constraints and irreversibilities associated with energy transfer through h_c and h_{eff} are the dominating system influences with Π_2 controlling overall performance in the designated process time Δt; these effects subsume heat and mass transport optimization in the reactors. This clearly occurs in the poor system as demonstrated in the previous discussion.

7. SUMMARY

This paper has described the reactor dynamics for coupled porous MH reactors over a complete cycle. The basic principles governing reactor design and optimization were discussed in Section 2. A formulation whose major assumption is local thermodynamic equilibrium was developed in Section 3. The qualitative features of the numerical solution in 1-D were discussed in Section 5. Values of Π_2 near unity are necessary (but

not sufficient) for high specific power and COP. Section 6 examined the transient fields and the basic mechanisms operating as a system of coupled reactors was optimized in the parameter Π_2 for the charging and cooling phases. It was found that the large ΔHs and rapid kinetics of MHs, often referred to as desirable characteristics, act in conjunction to produce sharp reaction fronts which remain close to heat transfer surfaces. In both coupled phases the reaction fronts occupy a much greater fraction of the reactor volume when Π_2 is increased. This allows a greater fraction of the absorbed hydrogen inventory to be exchanged in a given time Δt. It was also found that the initial transient period cannot be ignored.

The calculations demonstrate a profound asymmetry in the reactor dynamics between the regenerator and the refrigerator regardless of Π_2. The regenerator undergoes substantially greater fluctuations in temperature and pressure, as is well known. However, the large inhomogeneities and temporal variations of concentration have not been captured by less sophisticated models. This information is likely to influence future hydride selection for long-term operation.

The scope of this work has included optimization with respect to Π_2 which was identified as a key parameter in Section 2. Further work is required to address MH properties (ΔH, ΔS), reactant design (F_Q), alterations in the cycle and deviations from local thermodynamic equilibrium. Advanced optimization calculations would benefit greatly from further experimental effort placed on experimental evaluation of MH kinetics.

Acknowledgements—The first author wishes to acknowledge sustained financial support provided by a NASA Space Grant Fellowship. Additional resources were provided by Thermal Electric Devices Inc. Computational facilities were sponsored in part by the Phillips Laboratory, Air Force Material Command, USAF, under cooperative agreement number F29601-93-2-0001.

REFERENCES

1. Dantzer, P. and Orgaz, E., Thermodynamics of hydride chemical heat pump—II. How to select a pair of alloys. *International Journal of Hydrogen Energy*, 1986, **11**(12), 797–806.
2. Fujitani, S. *et al.*, Development of hydrogen-absorbing rare-earth-Ni alloys for a −20°C refrigeration system. *Journal of Alloys and Compounds*, 1993, **192**, 170–172.
3. Herold, K. E., Design challenges in absorption chillers. *Mechanical Engineering*, 1995, **117**(10), 80–83.
4. Meunier, F., Solid sorption: an alternative to CFCs. *Heat Recovery Systems and CHP*, 1993, **13**(4), 289–295.
5. Rockenfeller, U., Solid–gas chemisorption: efficient HVAC&R without CFCs. *ASHRAE Journal*, 1992, March, 54–58.
6. Choi, H. and Mills, A. F., Metal hydride heat pumps for upgrading spacecraft waste heat. *Journal of Thermophysics*, 1991, **5**(2), 135–141.
7. Bowman, R. C., Fabrication and testing of the metal hydride sorbent bed assembly for a periodic 10 K sorption cryocooler. In *Cryocoolers* 8, ed. R. G. Ross. Plenum Press, 1995, pp. 601–608.
8. Kim, K. J., Feldman, K. T., Lloyd, G., Razani, A. and Shanahan, K. L., Performance of high power metal hydride reactors. *International Journal of Hydrogen Energy*, 1997 (in press).
9. Lloyd, G., Razani, A. and Feldman, K. T., Design of absorption hydride heat pump: use of 1-D model in focusing media development and refinement. *Proceedings of the ASME International Mechanical Engineering Congress and Exp., San Francisco*, 1995, AES-Vol. 34, 1995, pp. 205–210.
10. Spinner, B., Ammonia-based thermochemical transformers. *Heat Recovery Systems and CHP*, 1993, **13**(4), 301–307.
11. Huston, E. L. and Sandrock, G. D., Engineering properties of metal hydrides. *Journal of Less-Common Metals*, 1980, **74**, 435–443.
12. Kuznetsov, A. V. and Vafai, K., Analytical comparison and criteria for heat and mass transfer models in metal hydride packed beds. *International Journal of Heat and Mass Transfer*, 1995, **38**(5), 2873–2884.
13. Kuznetsov, A. V., Investigation of the working cycle of a metal hydride heat transformer for upgrading waste heat. *Proceedings of the Institute of Mechanical Engineers: Journal of Power and Energy*, 1996, **210**(A2), 157–163.
14. Gopal, M. R. and Murthy, S. S., Performance of a metal hydride cooling system. *International Journal of Refrigeration*, 1995, **18**(6), 413–421.
15. Kang, B. H. and Kuznetsov, A., Thermal modelling and analysis of a metal hydride chiller for air-conditioning. *International Journal of Hydrogen Energy*, 1995, **20**(8), 665–674.
16. Gopal, M. R. and Murthy, S. S., Predictions of metal-hydride refrigerator performance based on reactor heat and mass transfer. *International Journal of Hydrogen Energy*, 1995, **20**(7), 607–614.
17. Jemni, A. and Nasrallah, S. B., Study of two-dimensional heat and mass transfer during desorption in a metal hydrogen reactor. *International Journal of Hydrogen Energy*, 1995, **20**(11), 881–891.
18. Lloyd, G., Razani, A. and Feldman, K. T., Fundamental issues involved in a theoretical description of the heat and hydrogen transfer occurring in coupled porous metal hydride reactors. *Proceedings of the ASME International Mechanical Engineers Congress and Exp.*, HTD-Vol. 321/FED-Vol. 233. San Francisco 1995, pp. 671–681.
19. Gambini, M., Metal hydride energy systems performance evaluation. Part A: dynamic analysis model of heat and mass transfer. *International Journal of Hydrogen Energy*, 1994, **19**(1), 67–80.
20. El-Osairy, M. A., El-Osery, I. A., Metwally, A. M. and Hassan, M. A., Two-dimensional dynamic analysis of metal hydride hydrogen energy storage conduction bed models. *International Journal of Hydrogen Energy*, 1993, **18**(6), 517–524.
21. Sun, D. and Deng, S., Numerical solution of the two-dimensional non-steady heat and mass transfer problem in metal hydride beds. *International Journal of Hydrogen Energy*, 1990, **15**(11), 807–816.
22. Choi, Hae-Jin, Hydride heat pump for upgrading spacecraft waste heat. Ph.D. thesis, University of California, Los Angeles, CA, 1989.
23. Bjurström, H. and Suda, S., The metal hydride heat pump: dynamics of hydrogen transfer. *International Journal of Hydrogen Energy*, 1989, **14**(1), 19–28.
24. Mayer, U., Groll, M. and Supper, W., Heat and mass transfer in metal hydride reaction beds: experimental and theoretical results. *Journal of Less Common Metals*, 1987, **131**, 235–244.
25. Lloyd, G. M., Transient heat/mass transfer modeling of metal hydride cycles. M.S. thesis, University of New Mexico, Albuquerque, NM, 1994.
26. Kallweit, J. and Hahne, E., Effective thermal conductivity of metal hydride powders: measurements and theoretical modeling. *Heat Transfer* 1994; *Proceedings of the Tenth International Heat Transfer Conference*, **6**, 373–378.

27. Ron, M. and Josephy, Y., Development problems of metal hydride reaction beds. In *Proceedings of the International Workshop on Metal Hydrides for Hydrogen Storage, Purification, and Thermodynamic Devices*, ed. M. Groll, R. Werner. Stuttgart, Germany, 1988, pp. 43–53.
28. Kaviany, M., *Principles of Heat Transfer in Porous Media*. Springer, New York, 1991, p. 357.
29. Morrison, F. A., Transient gas flow in a porous column. *Industrial Engineering and Chemical Fundamentals*, 1972, **11**(2), 191–197.
30. Oran, E. S. and Boris, J. P., *Numerical Simulation of Reactive Flow*. Elsevier Science, Oxford, 1987, p. 66.
31. Gray, W. G., Comparison of finite difference and finite element methods. In *Fundamentals of Transport Phenomena in Porous Media*, ed. J. Bear and M. Y. Corapcioglu. Martinus Nijhoff Publishers, The Netherlands, 1984, pp. 899–952.
32. Schneider, G. E., Strong, A. B. and Yovanovick, M. M., Finite difference modelling of the heat conduction equation in general orthogonal curvilinear coordinates using Taylor series expansion. In *Advances in Computer Methods for Partial Differential Equations*, ed. R. Vichnevetsky, 1975, pp. 312–317.
33. Carnahan, B., Luther, H. A. and Wilkes, J. O., *Applied Numerical Methods*. Wiley, New York, 1969, p. 464.
34. Ron, M., A hydrogen heat pump as a bus air conditioner. *Journal of Less Common Metals*, 1984, **104**, 259–278.
35. Groll, M., Reaction beds for dry sorption machines. *Heat Recovery Systems and CHP*, 1993, **13**(4), 341–346.
36. Lloyd, G., Razani, A., Kim, K. and Feldman, K. T., Cooling power/efficiency diagrams for a compressor-driven metal hydride heat pump. *ASHRAE Transactions*, 1997, **103** (in press).
37. Wang-X. L. and Suda, S., Reaction kinetics of hydrogen-metal hydride systems. *International Journal of Hydrogen Energy*, 1990, **15**(8), 569–577.
38. McKinnon, W. R., Energy dissipation during phase conversion : application to calorimetry and hysteresis in metal hydrides. *Journal of Less Common Metals*, 1993, **91**, 293–307.
39. Flanagan, T. B. and Oates, W. A., The palladium–hydrogen system. In *Annual Review of Material Science*, ed. R. A. Huggins, Vol. 21. Annual Reviews Inc., Palo Alto, CA, 1991, pp. 269–304.
40. Wanner, M., Friedlmeier, G., Hoffmann, G. and Groll, M., Thermodynamic and structural changes of various intermetallic compounds during extended cycling in closed systems. *International Symposium on Metal-Hydrogen Systems*, Les Diablerets, Switzerland, August 25–30, 1996.
41. Lambert, S. W., Chandra, D., Cathey, W. N., Lynch, F. E. and Bowman, R. C., Investigation of hydriding properties of $LaNi_{4.18}Sn_{0.2}$, $LaNi_{4.27}Sn_{0.24}$, $La_{0.9}Gd_{0.1}Ni_{0.1}$ after thermal cycling and aging. *Journal of Alloys and Compounds*, 1992, **187**, 113–135.
42. Chao, B. H., Wang, H. and Cheng, P., Stagnation point flow of a chemically reactive fluid in a catalytic porous bed. *International Journal of Heat and Mass Transfer*, 1996, **39**(14), 3003–3019.
43. Land, N. S., *Compilation of NonDimensional Numbers*. NASA SP-274, 1972, pp. 27–28.
44. Lloyd, G. M., Razani, A. and Feldman, K. T., Transient heat/mass transfer modeling of coupled metal hydride reactors for a heat-driven refrigeration system. Paper #33b. *AICHE Summer National Meeting in Recent Advances in Multicomponent Multiphase Reacting Flows; Theory and Experiments*. AICHE, 345 East 47th Street, New York, 10017, 1995.